

LETTER TO THE EDITOR

Detection of CO₂ ice in the planetary nebula NGC 6302

Charmi Bhatt^{1,2}, Simon W. Cao¹, Jan Cami^{1,2}, Nicholas Clark¹, Pascale Ehrenfreund^{3,4}, Els Peeters^{1,2}, Mikako Matsuura⁵, G. C. Sloan^{6,7}, Harriet L. Dinerstein⁸, Patrick Kavanagh⁹, Kevin Volk⁶, Isabel Aleman¹⁰, Michael J. Barlow¹¹, Kay Justannont¹², Kathleen E. Kraemer¹³, Joel H. Kastner^{14, 15, 16}, Francisca Kemper^{17, 18, 19}, Hektor Monteiro^{5, 20}, Raghvendra Sahai²¹, N. C. Sterling²², Jeremy R. Walsh²³, L. B. F. M. Waters^{24, 25}, and Albert Zijlstra²⁶

(Affiliations can be found after the references)

ABSTRACT

Using JWST/MIRI observations, we report the detection of CO₂ ice in the dusty torus of the planetary nebula NGC 6302, an environment generally considered hostile to fragile molecular species and ices due to intense UV irradiation. This detection accompanies cold (20-50 K) gas-phase CO₂ along the same sightlines. The ice absorption profile exhibits a double-peak profile, a characteristic of pure, crystalline CO₂ ice. The CO₂ gas-to-ice ratio is more than an order of magnitude higher than in young stellar objects, pointing to distinct ice formation or processing mechanisms in evolved stellar environments. This discovery demonstrates that the dusty torus provides sufficient shielding to harbour ice chemistry, and that ice-mediated surface reactions must be incorporated into chemical models of planetary nebulae.

Key words. ISM: planetary nebulae - Astrochemistry - ISM: molecules - Infrared: ISM - Stars: Circumstellar matter

1. Introduction

During the asymptotic giant branch (AGB) phase, low- to intermediate-mass ($\sim 1-8 M_{\odot}$) stars experience substantial mass loss ($\sim 10^{-8}$ to $10^{-4} M_{\odot} \text{ yr}^{-1}$; see Höfner & Olofsson 2018), and as this stellar material expands outward it cools, enabling the formation of a wide variety of molecules and dust grains. As the central star evolves through the post-AGB phase, the effective temperature increases rapidly and when $T_{\text{eff}} \gtrsim 20,000\text{K}$, intense UV radiation begins to ionize the circumstellar material, forming a planetary nebula (PN; plural: PNe) – a generally hostile environment where photo-dissociation, photo-evaporation and energetic stellar outflows cause a dramatic decline in the molecular diversity compared to the AGB phase (Agúndez 2022). However, our understanding of the chemical pathways operating in PNe remains incomplete. JWST observations have only just begun revealing some of these key processes. Among the objects observed, the Butterfly Nebula (NGC 6302, a complex bipolar PN) has emerged as a particularly intriguing laboratory for investigating complex chemical pathways in PNe due to its extreme environment and surprisingly rich chemistry.

NGC 6302 is an oxygen-rich (O-rich) evolved object that was never a carbon star (Wright et al. 2011; Matsuura et al. 2025). Yet recent JWST/MIRI observations have revealed the presence of CH₃⁺ (Bhatt et al. 2025b), a key driver of organic chemistry (Smith 1992; Herbst 2021; Berné et al. 2023; Zannese et al. 2025; Goicoechea et al. 2025) whose formation is enabled by the intense UV radiation from the central star. Moreover, the widespread presence of polycyclic aromatic hydrocarbons (PAHs) in this object (Matsuura et al. 2025) is also puzzling, and large variations in its spectral features point to in-situ formation and/or processing (Clark et al., in prep). Both findings demonstrate that this extreme environment supports rich chemical processes, and NGC 6302 thus represents a particularly intriguing laboratory for investigating some of the complex chemical pathways in PNe. Here, we report another surprising discovery: the clear spectral signatures of cold CO₂ gas and the

presence of CO₂ ice features, marking the first detection of CO₂ ice in a PNe.

2. The torus of NGC 6302

NGC 6302 exhibits bright east-west oriented bipolar lobes bisected by a massive dusty torus (oriented north-south; see Fig. A.1) that appears as a dark lane obscuring the central star at visible and near-infrared (IR) wavelengths (Kastner et al. 2022). ALMA ¹²CO J=3–2 observations reveal that the torus is non-Keplerian and radially expanding at 8 km s⁻¹, with a kinematical age of 5000–7500 years (Peretto et al. 2007; Santander-García et al. 2017). JWST mid-IR observations show that the torus is flared and warped, extending to a radius of 5.5'' (5700 AU) at infrared wavelengths (Matsuura et al. 2025). The extinction in the torus at 5.9 μm yields $A_v > 76$ mag, indicating a (dust + gas) mass of 0.8–3 M_{\odot} and a hydrogen density of $n_H \sim 6 \times 10^6 \text{ cm}^{-3}$ (Matsuura et al. 2025). ISO-SWS spectra of NGC 6302 reveal the presence of crystalline silicates and carbonates (Molster et al. 2001; Kemper et al. 2002b).

This work utilizes JWST MIRI/MRS observations (Wells et al. 2015; Argyriou et al. 2023) of NGC 6302 (program ID 1742; PI: M. Matsuura), covering the central star, torus, and innermost region of the bipolar lobes (Fig. A.1; see Matsuura et al. 2025, for more details). The data reduction was performed using JWST Calibration Pipeline version 1.16.1 and CRDS version 11.17.19 (see Matsuura et al. 2025 and Clark et al., in prep, for details on the data reduction).

3. Gas-phase CO₂ absorption

The JWST/MIRI MRS spectra towards the northern part of the torus (see Fig. A.1) reveal clear absorption features in the 14.8–15.2 μm range corresponding to the ν_2 bending mode of gas-phase CO₂ (see Fig. 1).

We calculated CO₂ model spectra as described in Cami et al. (2010), using the Carbon Dioxide Spectroscopic Database

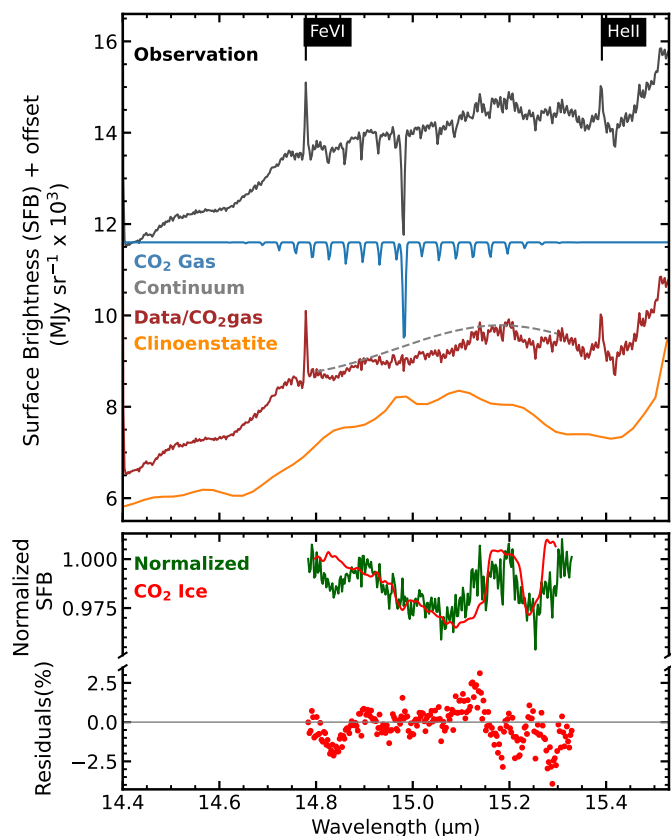


Fig. 1. Detection of CO₂ ice and gas. The black curve on top is the JWST/MIRI spectrum at the position indicated by the dot in Fig. A.1. Uncertainties on the surface brightness are $\sim \pm 40$ MJy sr⁻¹. The best-fit gas-phase model ($T_{\text{gas}} = 30$ K and $\log N = 16.8$ cm⁻²) is shown in blue. We divided out this model, resulting in the brown curve. The orange curve shows a single-temperature model for clinoenstatite emission. The grey dashed line is the continuum we adopt to analyse the ice band. The green curve shows the normalized spectrum using that continuum. The red curve is a laboratory spectrum for CO₂ ice (CO:CO₂ 2:1 ice mixture at 80 K); and the bottom panel shows the residuals between the normalized spectrum (green) and the ice model (red).

(CDS) linelist for ¹²CO₂ (Tashkun & Perevalov 2010). We adopted Gaussian intrinsic line profile with a line width $b=1$ km s⁻¹ and smoothed and resampled the resulting spectra to match the JWST/MIRI resolution at 15 μm. We used a model grid that spans temperatures of 10–100 K (in 10 K steps), and a logarithmic grid in column densities in the range of $\log N = 14$ –19 cm⁻² (in steps of $\log N = 0.1$). We also considered radial velocities in the range of -70 to -26 km s⁻¹ (in 1 km s⁻¹ steps) – a slightly wider velocity range than found by ALMA observations (Santander-García et al. 2017).

The CO₂ absorption occurs against a structured continuum. To determine this local continuum, we masked the narrow CO₂ absorption features and fitted a polynomial to the spectra. We then used this continuum to normalize the observed spectrum (see Fig. B.1) and performed a least-squares minimization at each pixel to simultaneously determine the excitation temperature, column density, and radial velocity of gas-phase CO₂. We determined the 1σ uncertainties on those best-fit parameters from the χ^2 hypersurface. The LTE CO₂ slab models generally reproduce the absorption very well (see Fig. 1). The CO₂ gas is cold everywhere we detect it, with temperatures in a narrow range of 20–50 K (with typical uncertainties of ± 10 K; Fig. A.2) for the majority of the spaxels. Column densities of

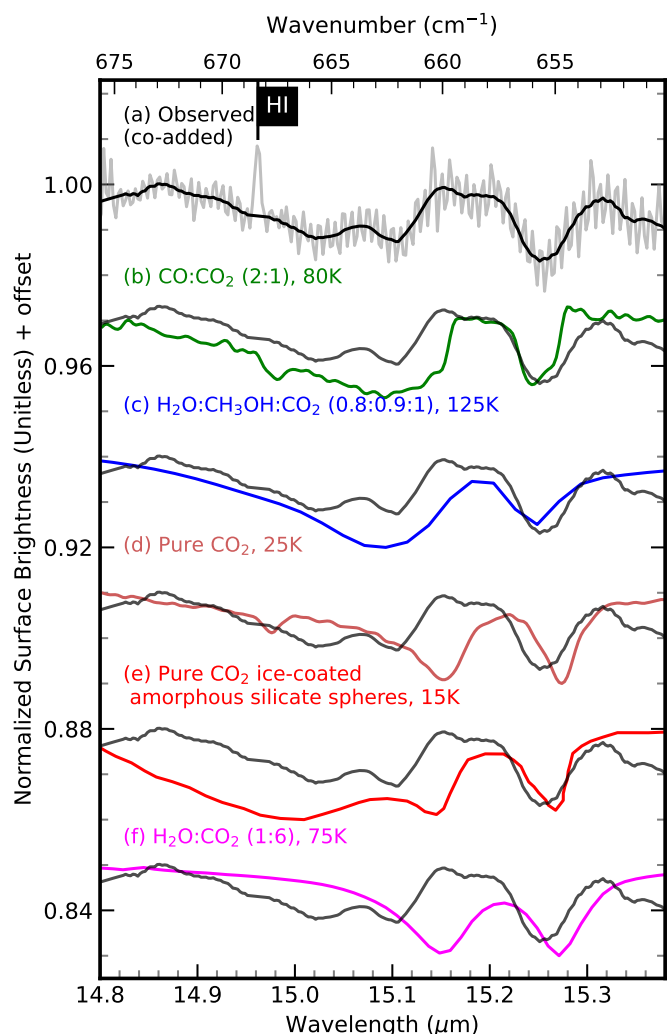


Fig. 2. Comparison of observational and laboratory ice spectra. (a) Co-added CO₂ absorption profile across all pixels with detectable CO₂ (gray), with the smoothed profile after masking the H I line at 14.96 μm overplotted in black. Laboratory spectra: (b) CO:CO₂ (2:1) at 80 K (green); (c) H₂O:CH₃OH:CO₂ (0.8:0.9:1) at 125 K (blue); (d) pure CO₂ at 25 K (brown); (e) pure CO₂ on amorphous silicate spheres at 15 K (red); (f) H₂O:CO₂ (1:6) at 75 K (pink).

this cold CO₂ gas increase smoothly by over an order of magnitude from the outer edge ($\log N = 15.2 \pm 0.1$ cm⁻²) to the torus midplane ($\log N = 16.8 \pm 0.1$ cm⁻²; Fig. A.1). For most pixels, the derived radial velocities, in the barycentric reference frame, range from -55 to -30 km s⁻¹ (with typical uncertainties of ± 3 km s⁻¹), similar to the range (-40 to -30 km s⁻¹) found using ALMA ¹²CO J=3–2 observations (Santander-García et al. 2017). We also detect much weaker spectral features of gas-phase ¹³CO₂ (see Appendix B).

4. Detection of CO₂ ice

The cold gas-phase CO₂ is located in the dusty torus of NGC 6302; this co-existence of dust and cold CO₂ gas mirrors conditions in envelopes of young stellar objects (YSOs) where CO₂ forms on cold dust grains, produces ice mantles, and desorbs when the temperature rises above the sublimation threshold. CO₂ ice formation thus appears plausible in NGC 6302 as well,

and we therefore searched for the characteristic ν_2 bending mode at $\sim 15.2 \mu\text{m}$ in the MIRI data.

To isolate potential ice absorption, we first divided the observations by the best-fit CO₂ gas model (see Fig. 1). The resulting spectrum (brown curve in Fig. 1) reveals a structured continuum containing spectral features from crystalline silicates (Molster et al. 2001; Kemper et al. 2002b,a). This complexity introduces significant uncertainty in continuum placement. Comparison with laboratory spectra shows that clinoenstatite in particular bears similarities to the spectrum (see Fig. C.1) and produces a strong absorption band at $\sim 15.4 \mu\text{m}$ that overlaps with the expected CO₂ ice band (Fig. 1). Despite this contamination, we identify two key signatures of CO₂ ice: (1) a shallow, broad absorption between ~ 14.9 - $15.15 \mu\text{m}$, and (2) a second absorption between ~ 15.2 - $15.3 \mu\text{m}$. This characteristic double-peak structure matches laboratory CO₂ ice spectra and is clearly distinct from the single, deeper clinoenstatite band at $15.4 \mu\text{m}$ or its weaker features. We fitted a local continuum (grey curve in Fig. 1) to bracket these CO₂ features while avoiding regions dominated by silicate absorption. Given the dust complexity and continuum uncertainties, we cannot perform detailed ice mixture decomposition. However, the distinctive double-peak signature provides robust identification of CO₂ ice despite the challenging spectral environment.

To improve the signal-to-noise ratio, we co-added spectra from all spaxels containing gas-phase CO₂ (resulting in the grey curve in Fig. 2a). The co-added spectrum reveals residual fringes that are not fully corrected by the MIRI data reduction pipeline. We applied a Savitzky-Golay filter (Savitzky & Golay 1964; Luo et al. 2005) to smooth out these fringes (black curve in Fig. 2a). The resulting co-added spectrum reveals a clear double-peaked feature where $\sim 15.05 \mu\text{m}$ feature is further split into two components and shows a broad blue wing.

Analysis of CO₂ ice absorption profiles in YSOs typically involves fitting a linear combination of five unique components to the data, each attributed to CO₂ in a different chemical environment (Pontoppidan et al. 2008; Brunken et al. 2024, 2025; Potapov et al. 2025). However, this approach is not suitable for our data. Individual spaxels lack sufficient S/N for reliable component decomposition, while the co-added spectrum represents a spatial average over disparate sightlines with varying physical conditions, making the interpretation of fitted components ambiguous. Given the continuum uncertainties described above and possible contamination from dust features, we instead rely on direct comparison with laboratory spectra to identify the presence of CO₂ ice.

We compared the observed $15.2 \mu\text{m}$ absorption profile with laboratory spectra from the Leiden Ice Database for Astrochemistry¹, including pure CO₂ ice and mixtures with CO, H₂O, CH₃OH, and other species at various temperatures. The observed double-peak structure best resembles CO:CO₂ (2:1) at 80 K and H₂O:CH₃OH:CO₂ (0.8:0.9:1) at 120 K (Fig. 2 Ehrenfreund et al. 1999; van Broekhuizen et al. 2006), reproducing the characteristic peak positions and relative intensities. Spectra of pure CO₂ ice and H₂O:CO₂ mixture also show a double peak feature but lack a broad blue wing (at $\sim 15.15 \mu\text{m}$). A model of pure CO₂-ice coated amorphous silicate spheres (Poteet et al. 2013) better resembles our profile with its triple-peak structure and broad blue wing. While Poteet et al. (2013) presented a model at 15 K only, their tabulated peak positions show decreasing peak separation with increasing temperature, suggesting that higher-temperature models would provide a better match to our observations. Given

that the exact profile is sensitive to the grain shape, size distribution and ice composition, we cannot reliably determine the specific ice mixture or temperature from our data, but the $15.2 \mu\text{m}$ feature confirms the presence of CO₂ ice in the torus of NGC 6302.

We calculated the average column density of CO₂ ice from the co-added and smoothed spectrum as $N_{\text{ice}} = \frac{\int \tau_\nu d\nu}{A}$ where $\int \tau_\nu d\nu$ is the integrated optical depth and A is the band strength. We used a value of $A = 1.6 \times 10^{-17} \text{ cm molecule}^{-1}$ (Bouilloud et al. 2015), and derive $N_{\text{ice}} \approx (1 \pm 0.3) \times 10^{16} \text{ cm}^{-2}$. The uncertainty here accounts for observational error.

5. Discussion

Molecular ices (such as H₂O, CO, CO₂, CH₄) are abundant in cold, shielded environments including dense molecular clouds, envelopes of YSOs, and protoplanetary disks (Boogert et al. 2015; Cuppen et al. 2024). Conditions required for the formation of H₂O ice are also met in dense AGB and post-AGB outflows as suggested by observations (Smith et al. 1988; Omont et al. 1990; Sylvester et al. 1999; Hoogzaad et al. 2002; Sahai et al. 2003; Manteiga et al. 2011). However, PNe present much harsher conditions due to the intense UV fields from the central star, making ice formation or survival generally infeasible (Dijkstra et al. 2006). Indeed, only three PNe show H₂O ice: CPD-56°8032 (Cohen et al. 1999), NGC 6537 (Molster et al. 2002), and NGC 6302 (Molster et al. 2001), all characterized by massive dusty tori providing exceptional shielding.

Our detection of CO₂ ice in NGC 6302 represents the first identification of an ice species more volatile than H₂O in any PN. Ice mantle formation depends on the balance between condensation and desorption, which varies with the binding energy of involved species, grain surface composition, and local physical conditions. For example, H₂O (the most abundant astrophysical ice) has highest binding energy and can typically remain in solid state at temperatures up to 150 K. On the other hand, CO₂ and CO have lower binding energies and thus desorb (in pure form) at 70-90 K and 20-30 K, respectively (Minissale et al. 2022). The detection of CO₂ ice therefore indicates both sufficient shielding and relatively cold temperatures in NGC 6302's torus.

JWST's high spatial resolution revealed that extinction toward the NGC 6302 torus ($A_V > 76 \text{ mag}$; Matsuura et al. 2025) is an order of magnitude higher than previously inferred from optical/near-IR observations ($A_V \approx 6 - 8 \text{ mag}$; Matsuura et al. 2005; Wright et al. 2011). This extreme shielding protects the ice from the central star's intense UV field ($T_{\text{eff}} \approx 220,000 \text{ K}$), allowing CO₂ ice to survive. While NGC 6302 may represent an extreme case, dense dusty tori are common around evolved stars, particularly in binary systems (Izzard & Jermyn 2023, and references therein), suggesting molecular ices may be more prevalent in these environments than previously recognized. JWST/MIRI's spatially resolved spectroscopy can now identify such highly shielded regions and assess the prevalence of ices in other PNe.

The observed CO₂ ice profile exhibits double-peak structure, a characteristic of pure, crystalline CO₂ ice, suggesting that CO₂ is present either in the pure form or in a mixture that is thermally processed (see Fig. 2; Ehrenfreund et al. 1997a, 1998; van Broekhuizen et al. 2006; Poteet et al. 2013). The CO₂ gas-to-ice ratio ($N_{\text{gas}}/N_{\text{ice}}$) in NGC 6302 is ~ 1 , much higher than in YSOs (~ 0.02 - 0.15 ; An et al. 2009, 2011), indicating a fundamentally different formation pathway in PNe environments. CO₂ may have formed primarily in the gas phase during AGB/post-AGB phase (see e.g. Justtanont et al. 1998; Cami et al. 2000;

¹ https://icedb.strw.leidenuniv.nl/spectrum_data

Malek & Cami 2014) with subsequent freeze-out onto grains. While models of AGB outflows have successfully reproduced observed H₂O ice column densities by incorporating accretion of gas-phase H₂O by gas-grain collisions (Dijkstra et al. 2003; Van de Sande et al. 2019), extending such models to include freeze-out of CO₂ in PN environments represents an important avenue for future work.

The presence of CO₂ ice in the PNe environment has important implications for ISM enrichment. CO₂ ice facilitates the surface chemistry required for the formation of complex organic molecules such as formic acid HCOOH, glycolaldehyde CH₂OHCHO, and acetaldehyde CH₃CHO (Herbst & van Dishoeck 2009; Jin & Garrod 2020; Potapov & McCoustra 2021; Garrod et al. 2022). Once formed, UV processing of these ices can drive further chemical complexity and controlled release back to the gas-phase, suggesting that PNe may contribute to the interstellar reservoir of organic material. If these species survive the prevailing physical and chemical processing, they may ultimately be incorporated into new star-forming systems. Such chemistry must be included in current PN chemical models and ISM enrichment models.

To comprehend the full picture, characterizing the full ice inventory in NGC 6302 is critical. The most abundant ice species in astrophysical environments – H₂O, CO₂, CO, CH₃OH, and NH₃ – have strong near-infrared absorption bands accessible to JWST NIRSpec, which can also detect their gas-phase counterparts, providing complementary information on sublimation processes and the ice-gas balance. High spatial resolution observations would constrain the chemical pathways, temperature structure, and ice processing mechanisms, establishing whether ice chemistry is common in dense PN tori.

6. Conclusions

We report the detection of CO₂ ice in a planetary nebula through spatially resolved JWST/MIRI observations of NGC 6302. This discovery demonstrates that molecular ices can form and survive in the heavily shielded regions of massive circumstellar tori, challenging the prevailing view that planetary nebulae are hostile to ice chemistry. We find CO₂ gas and ice present along the same line-of-sight. The gas-to-ice ratio differs markedly from that observed in young stellar objects, pointing to distinct ice formation or processing mechanisms in evolved stellar environments. Characterizing the full ice composition (H₂O, CO, CH₃OH, NH₃) and spatial distribution through JWST NIRSpec observations will be essential for understanding the chemical complexity of these systems. This opens planetary nebulae as a frontier for ice chemistry. Ice surface chemistry—crucial for complex organic molecule formation—operates in these environments, and other massive dusty tori may harbour similar chemistry. Chemical models must incorporate ice-mediated pathways.

Acknowledgements. This work is based on observations made with the NASA/ESA/CSA James Webb Space Telescope. All of the data presented in this article were obtained from the Mikulski Archive for Space Telescopes (MAST) at the Space Telescope Science Institute. The data of this specific observing program can be accessed via doi:10.17909/s1rn-1t84. This study is based on the international consortium of ESSENcE (Evolved Stars and their Nebulae in the JWST era). This article/publication is based upon work from COST Action NanoSpace, CA21126, supported by COST (European Cooperation in Science and Technology). C.B., S.C., J.C., E.P. and N.C. acknowledge support from the University of Western Ontario, the Canadian Space Agency (CSA) [22JWGO1-22], and the Natural Sciences and Engineering Research Council of Canada. K.E.K. acknowledges support from grant JWST-GO-01742.010-A and H.L.D. from JWST-GO-01742.004 A. FK acknowledges support from the Spanish Ministry of Science, Innovation and Universities, under grant number PID2023-149918NB-I00. This work was also partly supported by the Spanish

program Unidad de Excelencia María de Maeztu CEX2020-001058-M, financed by MCIN/AEI/10.13039/501100011033.

References

- Agúndez, M. 2022, in European Physical Journal Web of Conferences, Vol. 265, European Physical Journal Web of Conferences, 00029
- An, D., Ramírez, S. V., Sellgren, K., et al. 2011, *ApJ*, 736, 133
- An, D., Ramírez, S. V., Sellgren, K., et al. 2009, *ApJ*, 702, L128
- Argyriou, I., Glasse, A., Law, D. R., et al. 2023, *A&A*, 675, A111
- Berné, O., Martin-Drumel, M.-A., Schroetter, I., et al. 2023, *Nature*, 621, 56
- Bhatt, C., Cami, J., Peeters, E., et al. 2025b, *Astrophysical Journal*, 995, 67
- Boogert, A. C. A., Gerakines, P. A., & Whittet, D. C. B. 2015, *ARA&A*, 53, 541
- Bouilloud, M., Fray, N., Bénilan, Y., et al. 2015, *MNRAS*, 451, 2145
- Brunken, N. G. C., Boogert, A. C. A., van Dishoeck, E. F., et al. 2025, *ACS Earth and Space Chemistry*, 9, 1992
- Brunken, N. G. C., van Dishoeck, E. F., Slavicsinska, K., et al. 2024, *A&A*, 692, A163
- Cami, J., van Malderen, R., & Markwick, A. J. 2010, *ApJS*, 187, 409
- Cami, J., Yamamura, I., de Jong, T., et al. 2000, *A&A*, 360, 562
- Cohen, M., Barlow, M. J., Sylvester, R. J., et al. 1999, *ApJ*, 513, L135
- Cuppen, H. M., Linnartz, H., & Ioppolo, S. 2024, *ARA&A*, 62, 243
- Dijkstra, C., Dominik, C., Bouwman, J., & de Koter, A. 2006, *A&A*, 449, 1101
- Dijkstra, C., Dominik, C., Hoogzaad, S. N., de Koter, A., & Min, M. 2003, *A&A*, 401, 599
- Ehrenfreund, P., Boogert, A. C. A., Gerakines, P. A., Tielens, A. G. G. M., & van Dishoeck, E. F. 1997a, *A&A*, 328, 649
- Ehrenfreund, P., Dartois, E., Demyk, K., & D’Hendecourt, L. 1998, *A&A*, 339, L17
- Ehrenfreund, P., Kerkhof, O., Schutte, W. A., et al. 1999, *A&A*, 350, 240
- Garrod, R. T., Jin, M., Matis, K. A., et al. 2022, *ApJS*, 259, 1
- Goicoechea, J. R., Pety, J., Cuadrado, S., et al. 2025, *A&A*, 696, A100
- Herbst, E. 2021, *Frontiers in Astronomy and Space Sciences*, 8, 207
- Herbst, E. & van Dishoeck, E. F. 2009, *ARA&A*, 47, 427
- Höfner, S. & Olofsson, H. 2018, *A&A Rev.*, 26, 1
- Hoogzaad, S. N., Molster, F. J., Dominik, C., et al. 2002, *A&A*, 389, 547
- Izzard, R. G. & Jermyn, A. S. 2023, *MNRAS*, 521, 35
- Jin, M. & Garrod, R. T. 2020, *ApJS*, 249, 26
- Justtanont, K., Feuchtgruber, H., de Jong, T., et al. 1998, *A&A*, 330, L17
- Kastner, J. H., Moraga Baez, P., Balick, B., et al. 2022, *ApJ*, 927, 100
- Kemper, F., Jäger, C., Waters, L. B. F. M., et al. 2002a, *Nature*, 415, 295
- Kemper, F., Molster, F. J., Jäger, C., & Waters, L. B. F. M. 2002b, *A&A*, 394, 679
- Luo, J., Ying, K., & Bai, J. 2005, *Signal Processing*, 85, 1429
- Malek, S. E. & Cami, J. 2014, *ApJ*, 780, 41
- Manteiga, M., García-Hernández, D. A., Ulla, A., Manchado, A., & García-Lario, P. 2011, *AJ*, 141, 80
- Matsuura, M., Volk, K., Kavanagh, P., et al. 2025, *MNRAS*, 542, 1287
- Matsuura, M., Zijlstra, A. A., Molster, F. J., et al. 2005, *MNRAS*, 359, 383
- Minissale, M., Aikawa, Y., Bergin, E., et al. 2022, *ACS Earth and Space Chemistry*, 6, 597
- Molster, F. J., Lim, T. L., Sylvester, R. J., et al. 2001, *A&A*, 372, 165
- Molster, F. J., Waters, L. B. F. M., Tielens, A. G. G. M., & Barlow, M. J. 2002, *A&A*, 382, 184
- Moraga Baez, P., Kastner, J. H., Bublitz, J., et al. 2026, *ApJ*, 998, 7
- Omont, A., Moseley, S. H., Forveille, T., et al. 1990, *ApJ*, 355, L27
- Peretto, N., Fuller, G., Zijlstra, A., & Patel, N. 2007, *A&A*, 473, 207
- Pontoppidan, K. M., Boogert, A. C. A., Fraser, H. J., et al. 2008, *ApJ*, 678, 1005
- Potapov, A., Linz, H., Bouwman, J., et al. 2025, *A&A*, 697, A53
- Potapov, A. & McCoustra, M. 2021, *International Reviews in Physical Chemistry*, 299
- Poteet, C. A., Pontoppidan, K. M., Megeath, S. T., et al. 2013, *ApJ*, 766, 117
- Sahai, R., Zijlstra, A., Sánchez Contreras, C., & Morris, M. 2003, *ApJ*, 586, L81
- Santander-García, M., Bujarrabal, V., Alcolea, J., et al. 2017, *A&A*, 597, A27
- Savitzky, A. & Golay, M. J. E. 1964, *Analytical Chemistry*, 36, 1627
- Smith, D. 1992, *Chemical Reviews*, 92, 1473, [_eprint: https://doi.org/10.1021/cr00015a001](https://doi.org/10.1021/cr00015a001)
- Smith, R. G., Sellgren, K., & Tokunaga, A. T. 1988, *ApJ*, 334, 209
- Sylvester, R. J., Kemper, F., Barlow, M. J., et al. 1999, *A&A*, 352, 587
- Tashkun, S. A. & Perevalov, V. I. 2010, in 11th Biennial HITRAN Conference, 3
- van Broekhuizen, F. A., Groot, I. M. N., Fraser, H. J., van Dishoeck, E. F., & Schlemmer, S. 2006, *A&A*, 451, 723
- Van de Sande, M., Walsh, C., Mangan, T. P., & Decin, L. 2019, *MNRAS*, 490, 2023
- Wells, M., Pel, J. W., Glasse, A., et al. 2015, *PASP*, 127, 646
- Wright, N. J., Barlow, M. J., Ercolano, B., & Rauch, T. 2011, *MNRAS*, 418, 370
- Zannese, M., Tabone, B., Habart, E., et al. 2025, *A&A*, 696, A99

-
- ¹ Department of Physics and Astronomy, University of Western Ontario, London, Ontario, Canada
 - ² Institute for Earth and Space Exploration, University of Western Ontario, London, Ontario, Canada
 - ³ Leiden Observatory, Leiden University, PO Box 9513, 2300 RA Leiden, The Netherlands
 - ⁴ Space Policy Institute, George Washington University, 20052 Washington DC, USA
 - ⁵ Cardiff Hub for Astrophysics Research and Technology (CHART), School of Physics and Astronomy, Cardiff University, The Parade, Cardiff CF24 3AA, UK
 - ⁶ Space Telescope Science Institute, 3700 San Martin Drive, Baltimore, MD 21218, USA
 - ⁷ Department of Physics and Astronomy, University of North Carolina, Chapel Hill, NC 27599-3255, USA
 - ⁸ Department of Astronomy, University of Texas at Austin, Austin, TX 78712, USA
 - ⁹ Department of Physics, Maynooth University, Maynooth, County Kildare, Ireland
 - ¹⁰ Laboratório Nacional de Astrofísica, Rua dos Estados Unidos, 154, Bairro das Nações, Itajubá, MG, 37504-365, Brazil
 - ¹¹ Department of Physics and Astronomy, University College London, Gower Street, London WC1E 6BT, United Kingdom
 - ¹² Chalmers University of Technology, Onsala Space Observatory, 439 92 Onsala, Sweden
 - ¹³ Institute for Scientific Research, Boston College, 140 Commonwealth Avenue, Chestnut Hill, MA 02467, USA
 - ¹⁴ Center for Imaging Science, Rochester Institute of Technology, Rochester NY 14623, USA
 - ¹⁵ School of Physics and Astronomy, Rochester Institute of Technology, Rochester NY 14623, USA
 - ¹⁶ Laboratory for Multiwavelength Astrophysics, Rochester Institute of Technology, Rochester NY 14623, USA
 - ¹⁷ Institut de Ciències de l'Espai (ICE, CSIC), Can Magrans, s/n, E-08193 Cerdanyola del Vallès, Barcelona, Spain
 - ¹⁸ ICREA, Pg. Lluís Companys 23, E-08010 Barcelona, Spain
 - ¹⁹ Institut d'Estudis Espacials de Catalunya (IEEC), E-08860 Castelldefels, Barcelona, Spain
 - ²⁰ Instituto de Física e Química, Universidade Federal de Itajubá, Av. BPS 1303 Pinheirinho, 37500-903 Itajubá, MG, Brazil
 - ²¹ Jet Propulsion Laboratory, 4800 Oak Grove Drive, California Institute of Technology, Pasadena, CA 91109, USA
 - ²² University of West Georgia, 1601 Maple Street, Carrollton, GA 30118, USA
 - ²³ European Southern Observatory, Karl-Schwarzschild Strasse 2, D-85748 Garching, Germany
 - ²⁴ Department of Astrophysics/IMAPP, Radboud University, PO Box 19 9010, 6500 GL Nijmegen, The Netherlands
 - ²⁵ SRON Netherlands Institute for Space Research, Niels Bohrweg 4, 2333 CA Leiden, The Netherlands
 - ²⁶ Jodrell Bank Centre for Astrophysics, Department of Physics and Astronomy, The University of Manchester, Oxford Road, Manchester M13 9PL, UK

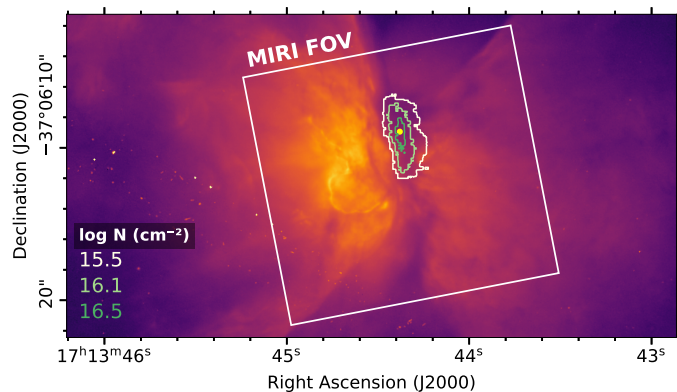


Fig. A.1. Location of CO₂ ice in NGC 6302. The image shows HST/WFC3 observations featuring filter F656N (Kastner et al. 2022), which traces H α emission. The JWST MIRI mosaic is indicated by the white frame. Contours show the column density of gas-phase CO₂, with corresponding log N values (cm⁻²) provided in the lower left. The yellow dot marks the pixel position (R.A. = 17^h:13^m:44.402^s, Dec. = -37°:06′:10.23 (J2000)) used to extract the spectra shown in the Figs. 1, 2, B.1, C.1.

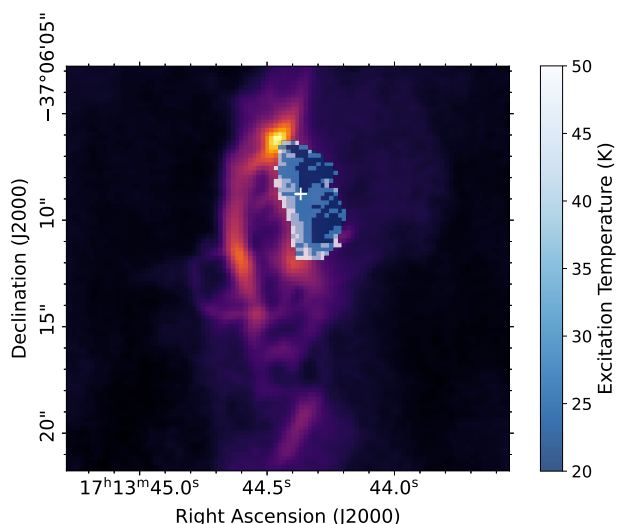


Fig. A.2. Spatial distribution of excitation temperature of CO₂ gas. The derived best-fit temperature of gas-phase CO₂ is mapped on the ALMA ¹²CO J=2–1 map (Moraga Baez et al. 2026). The temperature map reveals two blobs of colder CO₂ gas, which might indicate clumps in the torus, but needs further investigation.

Appendix A: Column density and excitation temperature of gas-phase CO₂

Fig. A.1 and Fig. A.2 shows the spatial variations in column density and excitation temperature of gas-phase CO₂. For details, see sec. 3.

Appendix B: Fitting ¹²CO₂ and ¹³CO₂

Along the same sightlines as ¹²CO₂, we detect much weaker spectral features due to gas-phase ¹³CO₂, which has a Q-branch at 15.42 μ m. We used the same fitting procedure as described in Sect. 3 to determine the column density of ¹³CO₂, with excitation temperatures and radial velocities tied to the ¹²CO₂ values for each pixel. An example fit is shown in Fig. B.1. From these column densities, we derived ¹²CO₂/¹³CO₂ (and thus ¹²C/¹³C) ratios in the range of 4–25, very similar to the range

(4–15) reported by Moraga Baez et al. (2026) for NGC 6302 using ALMA observations for ¹²CO/¹³CO, H¹²CO⁺/H¹³CO⁺, and H¹²CN/H¹³CN.

Appendix C: Clinoenstatite absorption

Fig.C.1 compares the observed spectrum with the modelled spectrum of clino-enstatite. While this represents a simplified approximation of the dust continuum (which depends of many factors), clino-enstatite clearly cannot reproduce the absorption feature underlying the gas-phase CO₂ line at around 15.2 μ m (see Sec.4).

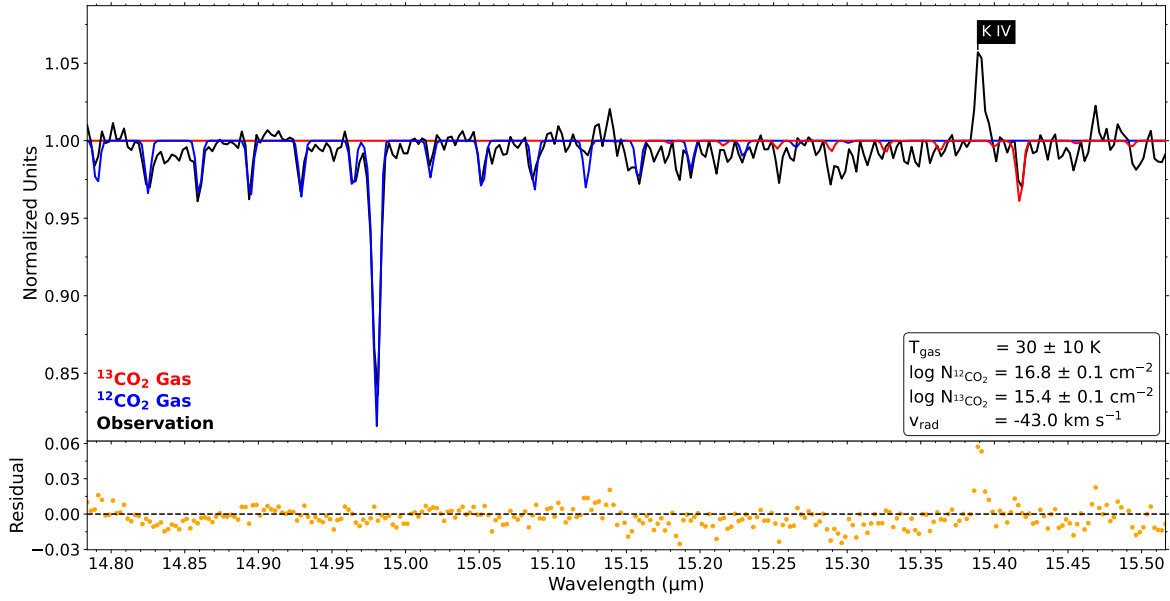


Fig. B.1. A representative fit of ¹²CO₂ and ¹³CO₂. Normalized observed spectrum towards the northern part of the torus facing us (R.A. = 17^h:13^m:44.402^s, Dec. = -37°:06′:10.23″ (J2000)) is shown in black and best-fit ¹²CO₂ model and ¹³CO₂ model are shown in blue and red, respectively.

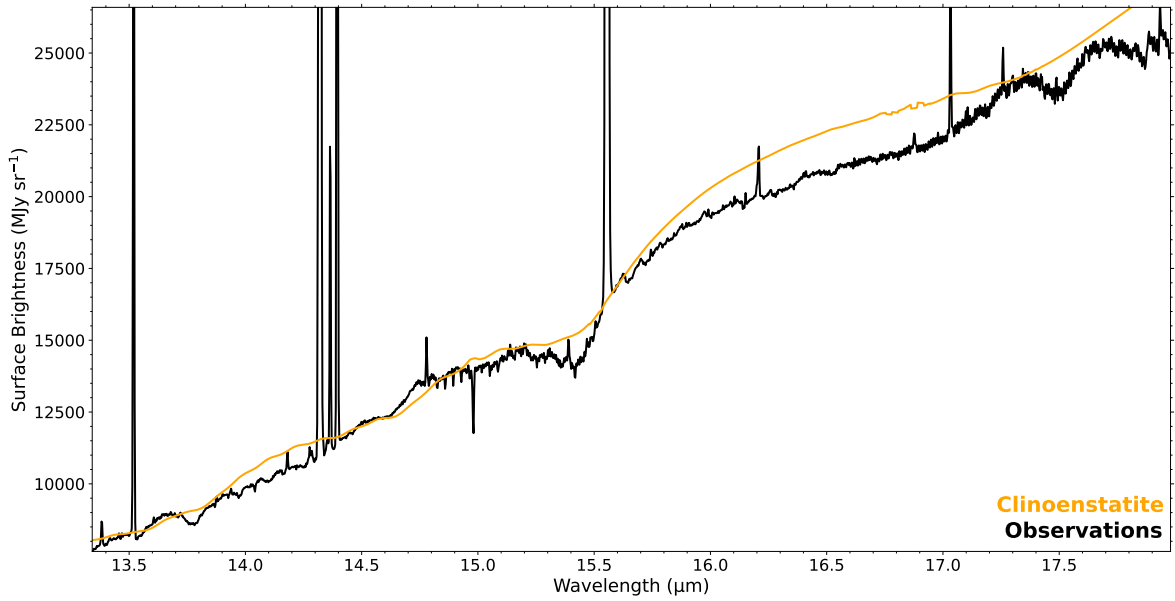


Fig. C.1. Comparison of observed spectrum with clino-enstatite model. The black curve represents the observed spectrum toward the same region as used to extract the spectrum in Fig. 1. The orange curve shows the modelled spectrum of clino-enstatite, derived using its optical depth profile under the assumption of blackbody emission for both the background continuum and mineral component.